Multi-morphology cellular structure design with smooth transition of geometry and homogenized mechanical properties between adjacent cells

Youngdoo Kim [a], Phong C.H. Nguyen [b], Hoon Kim [c,d], Young Choi [a,*]

[a] Department of Mechanical Engineering, Chung-Ang University, Seoul 06974, Republic of Korea
[b] School of Data Science, University of Virginia, Charlottesville 22903, VA, United States
[c] Graphy R&D Center, Graphy Inc., Seoul 08051, Republic of Korea
[d] Environmental Materials Science College of Agriculture & Life Science, Seoul National University, Seoul 08826, Republic of Korea

HIGHLIGHTS

- Multi-morphology cellular structure design method was proposed ensuring smooth transition of geometry and homogenized mechanical property between adjacent unit cells.
- Intermediate unit cells are optimized using a genetic algorithm under geometric and mechanical constraints.
- Continuity is ensured by the variable cutting level-set method with a level-set model composed of intermediate unit cells and a continuous variable cutting surface.
- Reduction of the maximum stress and improvement of elastic modulus were found via experiments and numerical tests.

GRAPHICAL ABSTRACT
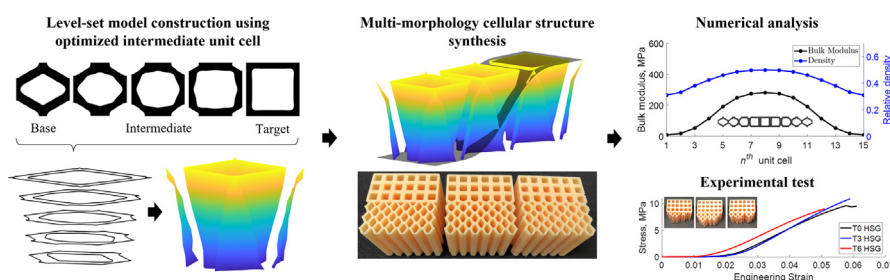
ABSTRACT

The recent development of additive manufacturing has led to an increased interest in the study of functionally graded cellular structures, which exhibit superior mechanical properties to the conventional uniform structures. However, connectivity is a critical problem that should be addressed, especially when multiple unit cell topologies are incorporated into a structure. In particular, inappropriate connectivity may cause stress concentration at the interfaces, reducing the structure's lifespan. This paper proposes a method to design multi-morphology cellular structures that ensures smooth transition of geometry and homogenized mechanical properties between adjacent unit cells. The proposed method uses a genetic algorithm to design intermediate unit cells between a base and a target unit cell. Moreover, a customized parametric unit cell representation supports the design process. An implicit modeling method is adopted to synthesize the explicit 3D models. Numerical analyses demonstrate that the proposed method guarantees smooth transitions of geometry at the interfaces, variations in density, and homogeneous mechanical properties. Moreover, experimental characterization resulted in an increase of 78.7% in the elastic modulus and a reduction of 54.9% in the maximum von Mises stress for the structure designed

---

* Corresponding author.
 E-mail addresses: yaedi5589@cau.ac.kr (Y. Kim), phongnguyen@virginia.edu (P.C.H. Nguyen), c12o2cl4@snu.ac.kr (H. Kim), yychoi@cau.ac.kr (Y. Choi).

with the proposed method when compared with that created using the conventional non-smoothing technique.

1. Introduction

Adaptation mechanisms in natural materials and structures enable outstanding mechanical behaviors and unique characteristics in diverse environments. For example, owing to its functionally graded elasticity and internal hardness, the dactyl club of the mantis shrimp resists strong impact [1]. Bamboo is well-known for functionally graded microstructures along the radial direction, which enhance its bending stiffness [2]. Horns, which play an important role during intraspecific combat, have microstructures and mechanical properties that adjust to fighting behaviors among different species [3].

Cellular structures can be classified into two types: stochastic and non-stochastic [4]. Stochastic cellular structures are those that cannot be characterized by a single unit cell. Commonly found in nature, as in the cases mentioned above, their functionally graded microstructures comprising various cell sizes enhance their effectiveness under given environments. This type has been recently studied using Voronoi tessellation [5,6]. In contrast, non-stochastic cellular structures, also known as periodic cellular structures, are defined by a unique cell topology. This type of structure has attracted the attention of researchers due to the feasibility of controlling its mechanical properties by appropriately manipulating the unit cell geometry [7,8].

Many researchers have focused on designing bioinspired microstructures and topology optimization to maximize engineering structural performance [1–3,9,10]. Sigmund [11] was the first to apply topology optimization to inverse homogenization problems, using it to design a 2D microstructure of square elements. Such an approach has been subsequently complemented by extreme thermal expansion [12], the ability to transport fluids [13], and piezocomposite structures [14]. The level-set method has also been adopted for microstructural design. This method realizes gradual changes in the geometries of the microstructures, thus ensuring easy topological transitions and smooth material boundaries while preventing stress concentrations at sharp corners [15–17]. Furthermore, Bézier and spline curves have been used to represent material boundaries within the microstructural configuration [18,19], providing higher compatibility with conventional computer-aided design (CAD) and finite element analysis (FEA) software [20,21].

Topology optimization has been recently applied to cellular structures. Nguyen et al. [22] simultaneously optimized functionally graded cellular structures (FGCSs) and their building orientation. In addition, they proposed an optimal design for the macroscale density distributions and the microstructure of a unit cell using microscale level-set descriptions [23]. Li et al. [24] developed an integrated structure–microstructure design approach based on the level-set method by dividing a structure into layers and optimizing the density of the unit cells in each layer to maximize structural performance. However, these studies did not consider the connectivity at the interfaces, which can cause stress concentration problems.

Inadequate connectivity between adjacent unit cells in an FGCS arises from scale separation [25] with stress concentration occurring at poorly connected or discontinuous interfaces and reducing the lifespan and stiffness of the FGCSs. These problems become critical if the adjacent unit cells have different topologies. There are three representative approaches to designing connectable cel-

lular structures. The first approach is to use the level-set model. Liu et al. [26] and Zong et al. [27] proposed a variable cutting (VCUT) level-set method to optimize both 2D and 3D FGCS. The VCUT level-set method synthesizes the microstructures by geometrically mapping a level-set model to a VCUT surface (VCUTS) and defining shared elements along the interface between adjacent unit cells to ensure at least C^0 continuity. Liu et al. [28] used Kriging metamodels for 3D cellular structure optimization, improving the VCUT level-set method and reducing its computational costs. The VCUT level-set method can provide an unlimited number of connectable unit cells by adjusting a VCUTS shape with a given level-set model. However, although it provides numerous cellular structures with smooth geometric transitions, studies [26–28] only considered a single type of unit cell for structural optimization. In contrast, Wang et al. [29] applied the VCUT level-set method to optimize a concurrent cellular structure comprising two different types of unit cells, whose implicit functions were interpolated to construct a level-set model. This implementation represented an important extension of the method but remained limited to using two geometrically similar unit cells.

The second approach to address connectivity problems is based on parametric interpolation. This approach has been widely used in generating intermediate (or hybridized) unit cells between two triply periodic minimal surface (TPMS) unit cells [30–33] that can be parametrically expressed. The intermediate unit cells are obtained as a weighted combination of the parametric description of the level-set models for the two or more TPMS unit cells. However, if the two unit cells do not share similar topologies, geometric aberrations and disconnection may occur, leading to stress concentration [32].

The last approach to ensure connectivity is by adjusting the microstructures within the unit cells. Zhou and Li [34] evaluated three strategies of this type to enforce the connectivity of cellular structures, with one of them, which entails the definition of non-design domains, having been extensively developed [35–37]. However, it may limit the corresponding design domain and unit cell optimization. Rodman et al. [38] and Garner et al. [39] designed connectable intermediate unit cells between two unit cells based on implicit shape interpolation by jointly optimizing each unit cell and its neighbors. Zobaer and Sutradhar [40] applied two-scale optimization to design 2D connectable intermediate unit cells. They reconstructed conventional unit cells by parametrically representing the microstructural geometries with superformula, before optimizing the intermediate unit cells through a geometrically and mechanically constrained genetic algorithm (GA). The connectivity was ensured after additional optimization to match the boundaries of adjacent unit cells. While the last two methods mentioned are applicable between two unit cells with different shapes or topologies, the whole process should be repeated if more intermediate unit cells are needed.

This paper proposes a novel method for designing multi-morphology cellular structures (MMCSs), which generates connectable MMCSs between two unit cells with different geometries while ensuring smooth transitions of geometry and homogenized mechanical properties between adjacent unit cells. The proposed method is not restricted to specific types of unit cells. Instead, it is applicable to any non-stochastic unit cell type. The overall design process is illustrated in Fig. 1. The present document is organized as follows. Section 2.1 describes parametric unit cell rep-
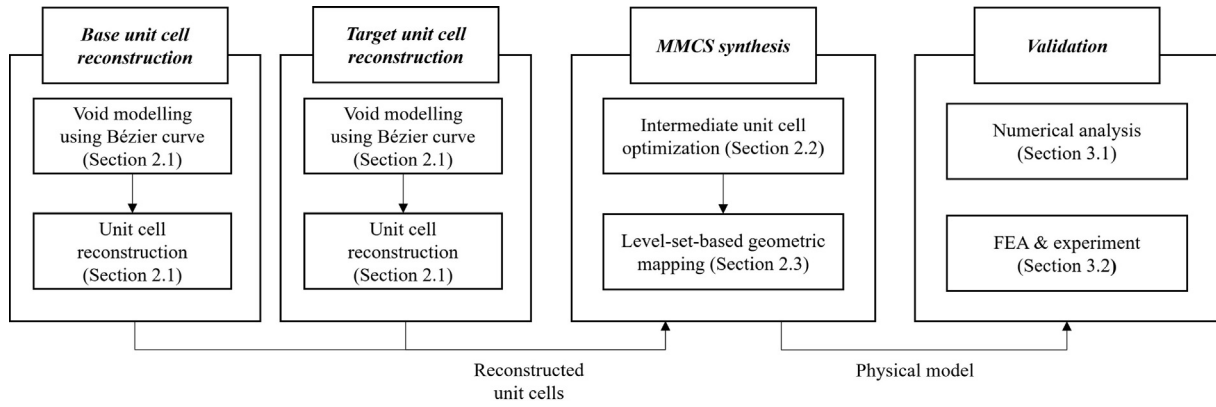
Fig. 1. Overview of the proposed MMCS design method.

resentation using customized Bézier curves. Section 2.2 discusses an intermediate unit cell optimization procedure using a GA under geometric and mechanical constraints. Section 2.3 explains geometric mapping with a VCUTS and a level-set model composed of the intermediate unit cells. Finally, Section 3 presents the results from the numerical analyses and experimental tests conducted to characterize the mechanical properties of MMCSs designed with the proposed method and to verify the capability of the latter to deliver smooth transitions of geometry and homogenized mechanical properties between adjacent unit cells.

2. Method

2.1. Parametric unit cell representation using Bézier curve

Bézier curves are widely utilized in computer-aided geometric design due to their flexibility in representing complex geometries and their compatibility with conventional CAD and FEA software [18,19]. In this paper, conventional unit cells are reconstructed by using constrained with Bézier curves to parametrically model the voids inside the unit cell.

Following the methodology explained [41], a unit cell can be implicitly represented by the following binary function:
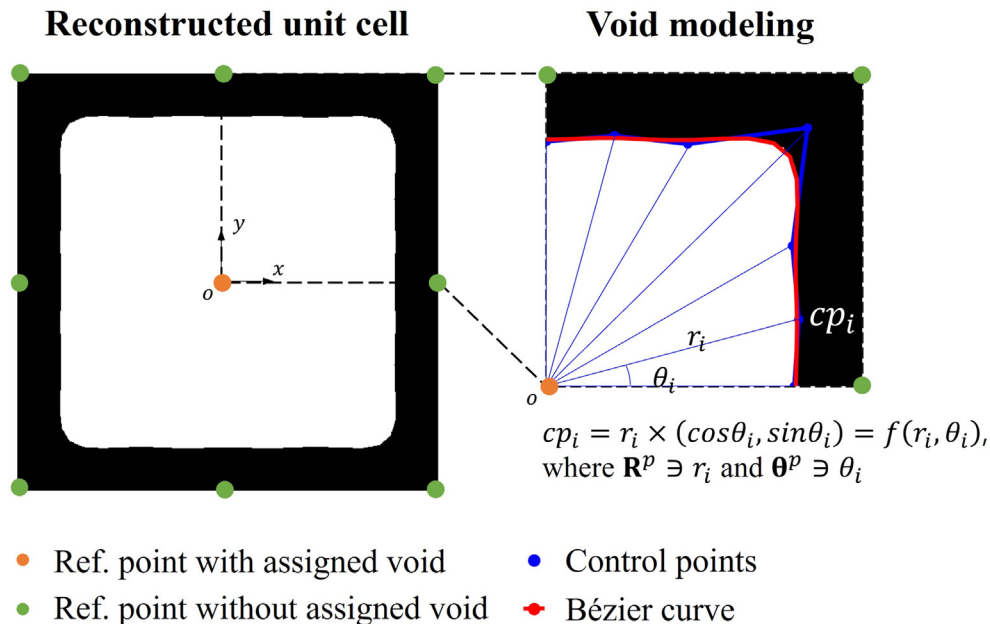
$$\begin{cases} \Phi(\mathbf{x}) = +1, & \text{if } \mathbf{x} \in \Omega \\ \Phi(\mathbf{x}) = 0, & \text{if } \mathbf{x} \in \partial\Omega \\ \Phi(\mathbf{x}) = -1, & \text{if } \mathbf{x} \in D \setminus \Omega \end{cases} \tag{1}$$

where $\mathbf{x}$ is a set of points in the discretized design domain D, Ω are the void regions and $\partial\Omega$ are the void boundary implicit curves. For a given implicit function Φ, $\partial\Omega$ is extracted using the MATLAB Image Processing Toolbox (MathWorks).

A unit cell generally comprises several voids, which should be separately modeled and represented during unit cell reconstruction. With the help of a void modeling process and coordinate system for void labeling [40], $\partial\Omega$ of a void is expressed by a parametric Bézier curve. As illustrated in Fig. 2, the coordinate system is composed of N uniformly distributed reference points in D, and each void is assigned to one reference point.

Once all the voids are parametrically modeled, a unit cell is reconstructed by the following Boolean operation:

$$\Phi_{unitcell} = D \cap \left(-\cup_{i=1}^{N} \Phi_i^p \right) \tag{2}$$

$$cp_i = r_i \times (cos\theta_i, sin\theta_i) = f(r_i, \theta_i),$$
$$\text{where } \mathbf{R}^p \ni r_i \text{ and } \boldsymbol{\theta}^p \ni \theta_i$$

- ● Ref. point with assigned void
- ● Ref. point without assigned void
- ● Control points
- ─●─ Bézier curve

Fig. 2. Square unit cell reconstructed with nine reference points.

where Φ_i^p is the implicit function of the ith parametrically represented void Ω_i^p. The negative sign for the union of Φ_i^p in Eq. (2) indicates the outside of Ω_i^p.

Fig. 2 illustrates a reconstructed square unit cell with a relative density of 0.4. The reconstructed unit cell is defined by nine reference points with orange and green points representing reference points with and without assigned voids, respectively. The parametrically expressed boundary $\partial\Omega^p$ is colored in red.

To reduce the computational cost, several assumptions are made for the parametric modeling of each void: 1) the shape of the void is axis-symmetric around its reference point (the local $x - y$ coordinate system), such that the void can be modeled by a closed Bézier curve; 2) the number of control points $\boldsymbol{cp}$ in the closed Bézier curve is predetermined; 3) $\boldsymbol{cp}$ in the local coordinate system associated to the void are expressed by a set of radii $\mathbf{R}^p$ and angles θ^p; and 4) if there is no void assigned to a reference point, $\mathbf{R}_i^p$

are set to small values such that Ω_i^p becomes negligible. The value of $\mathbf{R}_i^p$ when no void is assigned was set to 0.01 in this study. The axis-symmetric assumption reduces the range of θ^p from $0°$–$360°$ to $0°$–$90°$. $\mathbf{R}^p$ and θ^p are obtained based on the curve fitting process introduced in [40]. Fig. 3 shows the reconstruction of three types of conventional unit cells with the same relative density of 0.4.

2.2. Intermediate unit cell optimization

Intermediate unit cells are a sequence of microstructures that gradually morph between the geometries of the base and target unit cells. The basic idea behind designing intermediate unit cells is to transform the individual void of the base unit cell to that of the target unit cell by modifying parameters $\mathbf{R}_i^p$ under geometric and mechanical constraints [40]. To design M intermediate unit cells, the optimization problem is formulated as follows:
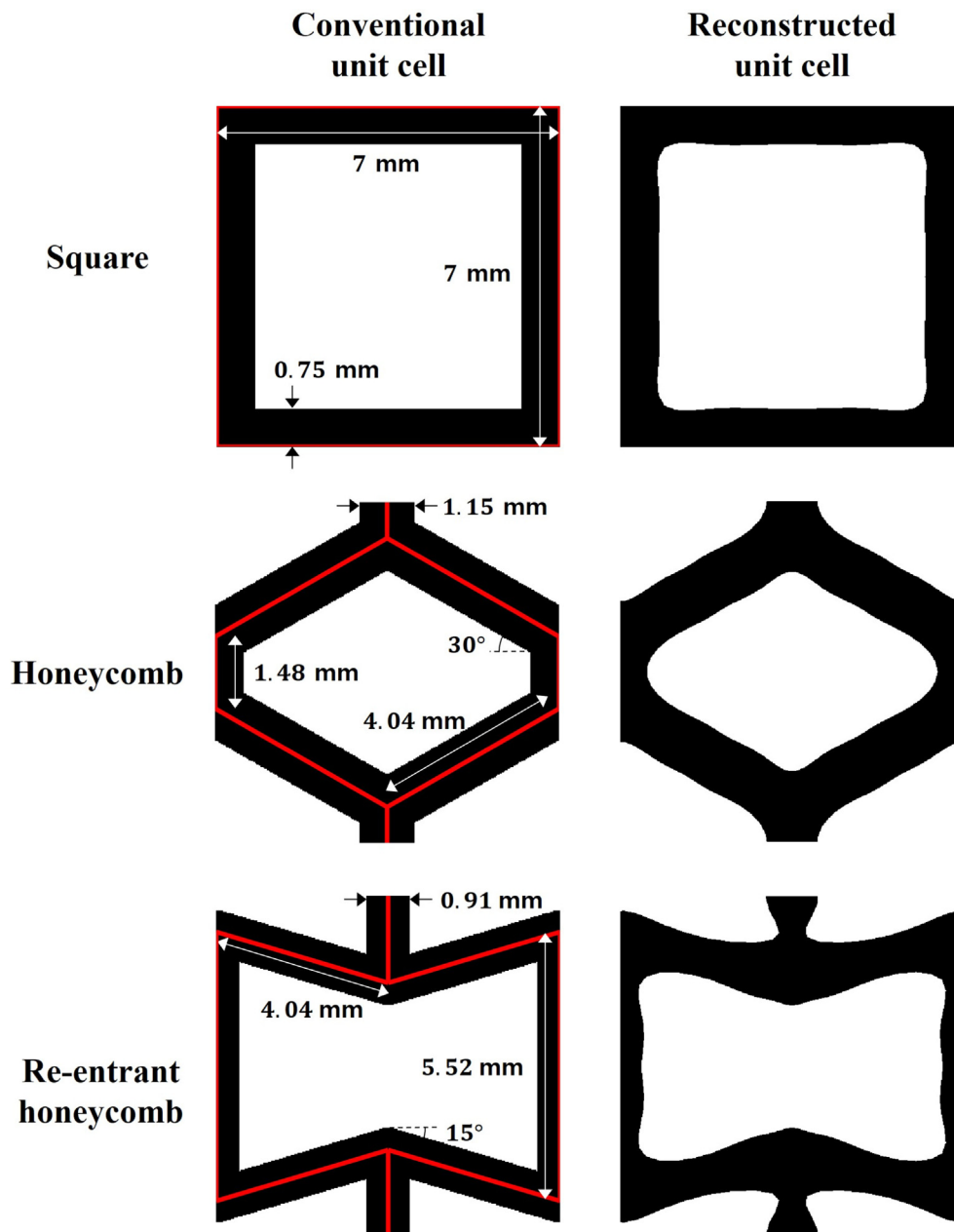

Fig. 3. Three types of conventional unit cells with a relative density of 0.4 (left) and their reconstructed models (right).

find $\mathbf{R}_{i,m}^{p}$

$$\min_{D} C = |P_T - P_m|$$

$$s.t. : \mathscr{I}_{\Phi_{i,m}^{p} \cap \Phi_{j,m}^{p}} = \varnothing, i, j \in N_r \, and \, i \neq j$$

$$: \mathbf{R}_{i,min}^{p} \leq \mathbf{R}_{i,m}^{p} \leq \mathbf{R}_{i,max}^{p}$$

$$: \sum_{e=1}^{n} \rho_e \, v_e \leq v_m$$

$$: c(t) \leq c_{max}, t \in [1, t_{max}) \tag{3}$$

where $\mathbf{R}_{i,m}^{p}$ are the parameter radii defining the ith void in the mth intermediate unit cell; P_T and P_m indicate specific mechanical property of the target and intermediate unit cells obtained by numerical homogenization [42], respectively; $\mathscr{I}_{\Omega_{i,m}^{p} \cap \Omega_{j,m}^{p}}$ denotes the similarity between $\Omega_{i,m}^{p}$ and $\Omega_{j,m}^{p}$ considering buffer distance κ, which is the minimum number of elements between $\Omega_{i,m}^{p}$ and $\Omega_{j,m}^{p}$ to prevent their intersection [40]; $\mathbf{R}_{i,min}^{p}$ and $\mathbf{R}_{i,max}^{p}$ are the lower and upper bounds of $\mathbf{R}_{i,m}^{p}$; v_e and ρ_e are the volume and relative density of the eth element; v_m is the maximum allowable volume fraction of an intermediate unit cell; $c(t)$ and c_{max} are the set of curvatures of the constrained Bézier curve and the user-defined maximum curvature, respectively; and t_{max} is determined by the number of control points and the order of the Bézier curve, which was set to 4 in this study. By introducing κ and c_{max}, a certain level of smoothness to the boundaries of each void Ω_i^{p} is guaranteed and self-intersection is prevented [40].

As $\mathbf{R}_{i,base}^{p}$ and $\mathbf{R}_{i,target}^{p}$ are known, they are used to define the $\mathbf{R}_{i,min}^{p}$ and $\mathbf{R}_{i,max}^{p}$ limits for each iteration. Linear interpolation is adopted for bounding the parameter domain $[\mathbf{R}_{i,base}^{p}, \mathbf{R}_{i,target}^{p}]$, which is then divided into $M+2$ nodes equally spaced by $\mathbf{R}_{i,diff}^{p}$. When designing the mth intermediate unit cell, the radii are bounded between $\mathbf{R}_{i,base}^{p} + (m+1) \times \mathbf{R}_{i,diff}^{p}$ and $\mathbf{R}_{i,base}^{p} + (m+2) \times \mathbf{R}_{i,diff}^{p}$. Similarly, v_m is set using a method analogous to that used to obtain the radii bounds, but the domain is $[v_{base}, v_{targ}]$, while c_{max} is chosen as 60 to derive a smooth boundary. As the optimization problem in Eq. (3) is nonlinear, gradient-based optimization tools are unsuitable. Instead, a GA is used to properly handle this nonlinear problem [40]. Fig. 4(a) shows optimized intermediate unit cells between a honeycomb and a square unit cell. These optimized intermediate unit cells are further processed with the VCUT level-set method to obtain a smooth geometric transition between adjacent unit cells.

2.3. Geometric mapping based on level-set model

The VCUT level-set method allows the synthesis of explicit geometric models for FGCSs with a level-set model that at least ensures C^0 continuity at the interfaces [26,27]. This implies that an MMCS can be synthesized with a level-set model φ, which
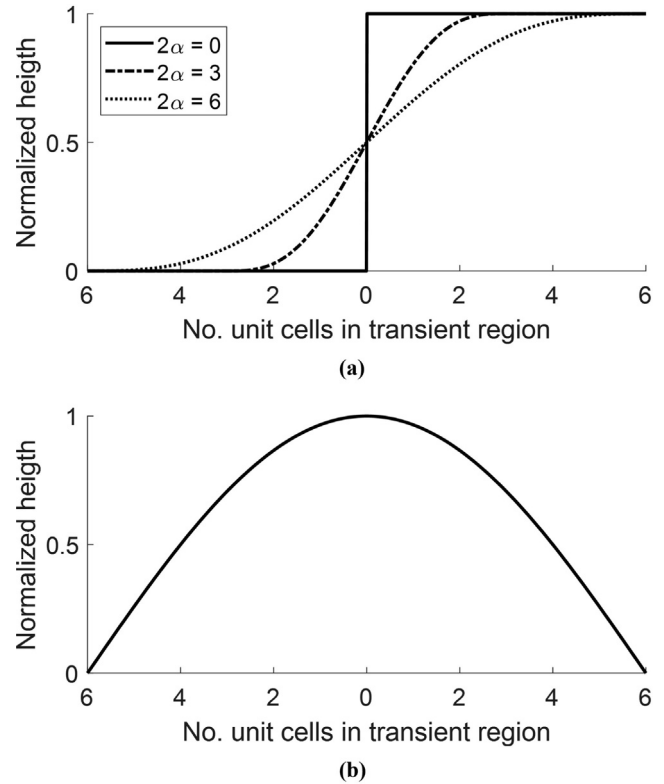

(a)

(b)

Fig. 5. Two types of VCUTSs: (a) smooth Heaviside function with different 2α values and (b) half sine function.
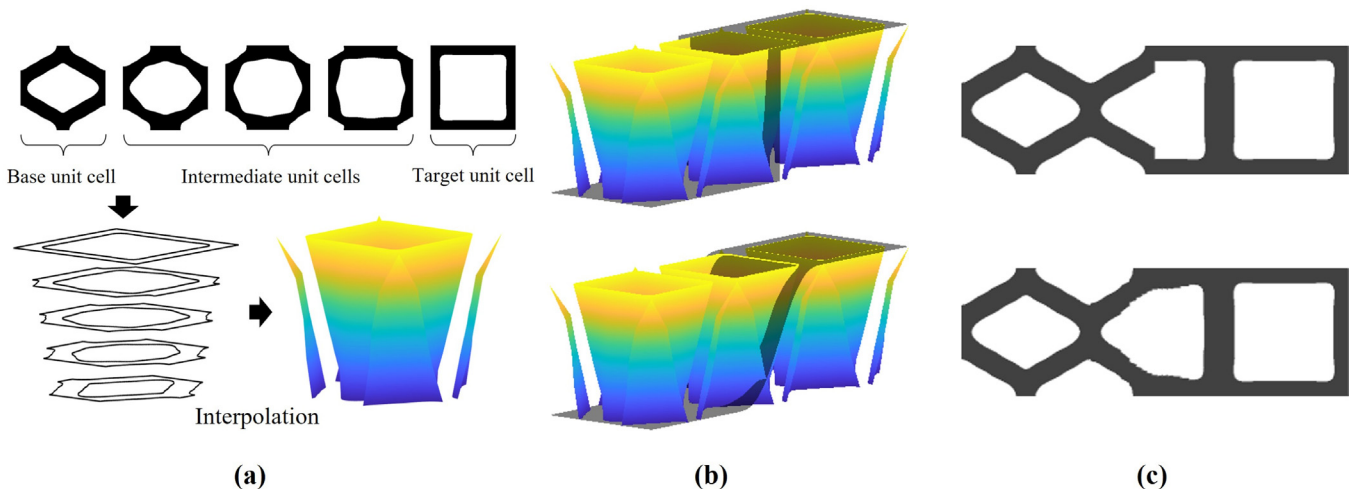

(a)

(b)

(c)

Fig. 4. MMCS synthesis process. (a) Level-set model construction, (b) populated level-set models with two different VCUTSs, and (c) synthesized MMCSs corresponding to each of the two VCUTSs.

properly represents a geometric morphing between two different unit cells. In this study, φ is constructed by stacking the intermediate unit cells and then linearly interpolating across their boundaries and the VCUT level-set method is used to generate MMCSs. Fig. 4 describes an MMCS synthesis process with a level-set model φ_{HS}, which contains the information for morphing from a honeycomb unit cell to a square unit cell, using two types of VCUTSs. These type of MMCSs are denoted HS MMCSs. By applying the differentiable VCUTS, MMCSs are smoothly connected at their interface.

3. Experimental study

Experimental test and FEA were conducted to verify the delivery of smooth transitions of geometry and homogenized mechanical properties by the proposed MMCS design method using both density and unit cell grading. To clearly distinguish various MMCSs in this study, several abbreviations are made. An HSG MMCS represents an MMCS morphed from a honeycomb unit cell with a relative density of 0.3 to a square unit cell with a relative density of 0.5. An HS MMCS without density grading, i.e., where the relative density remains constant at 0.4, is denoted HSU MMCS. Similarly, an RHU MMCS is a constant density MMCS morphed between a re-entrant honeycomb unit cell and a honeycomb unit cell.

To balance the tradeoff between computational cost and unit cell representation accuracy, θ^p were set to [0°, 15°, 30°, 45°, 60°, 90°], and D was discretized in 60×60 elements at the microscale. These two variables are directly related to the computational time and resources required for parametric modeling, numerical homogenization, and intermediate unit cell optimization. Owing
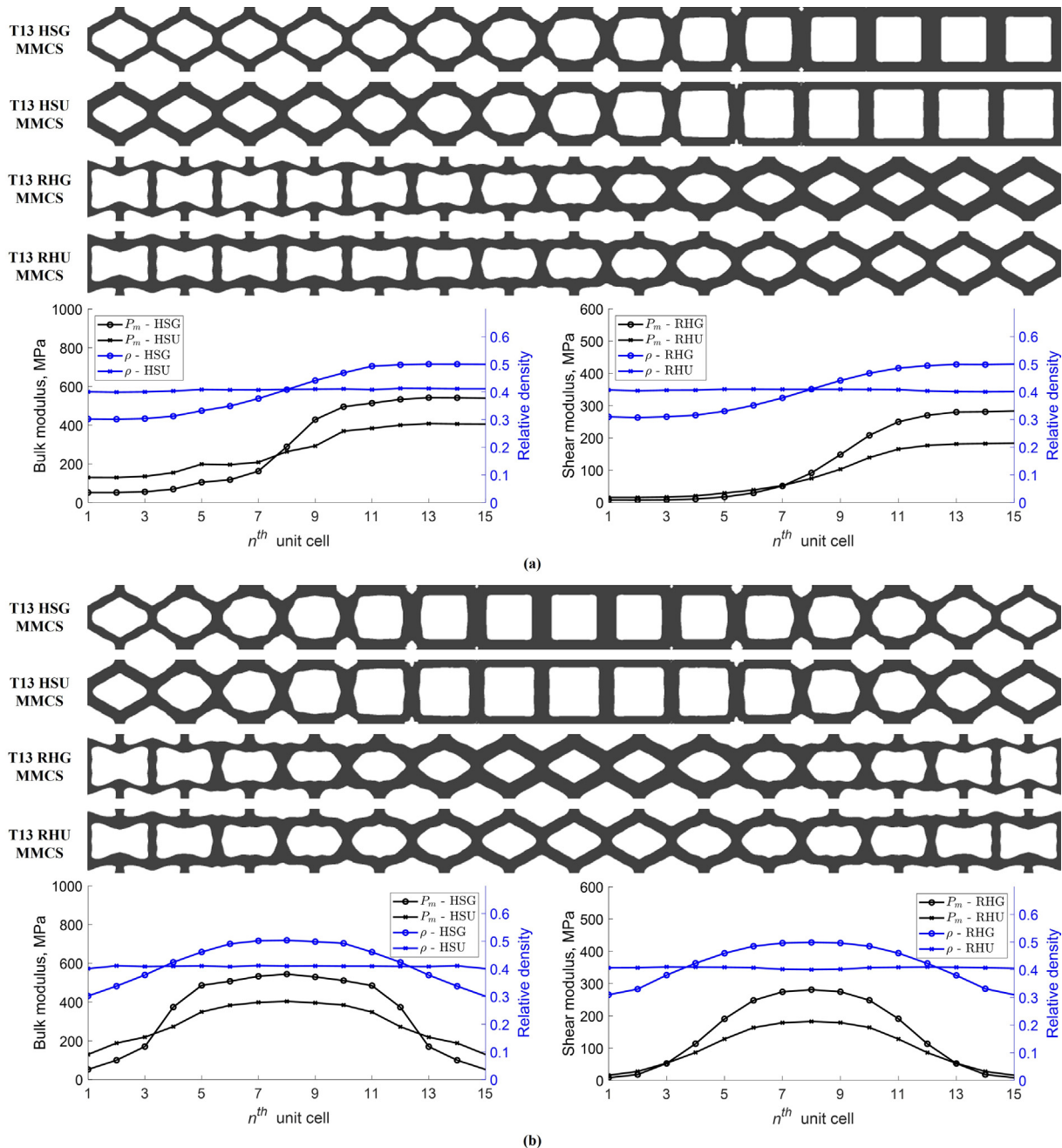

Fig. 6. Variations in the geometry and mechanical properties of 15×1 HS and RH MMCSs mapped through different VCUTSs across 13 transient unit cells: (a) smooth Heaviside VCUTS and (b) half-sine VCUTS. The geometric configurations are shown above, and the bulk/shear modulus and density of the unit cells are shown below.

to the advantage of parametric unit cell representation [40,43], a design domain D' discretized in 75 × 75 elements was utilized for the geometric mapping process to achieve an adequate geometric accuracy for the finite elements analyses, which is explained in Section 3.2. The buffer distance κ was set as twice the distance between two consecutive unit cells, and the population and generation of the GA for optimization of the intermediate unit cells were set to 2000 and 20, respectively. A laboratory computer with a 16-core 3.40 GHz AMD Ryzen processor and 64 GB of RAM was utilized for the computations.

3.1. Design examples

For the VCUTSs, a smooth Heaviside and half-sine functions were selected, as shown in Fig. 5. The length of the transient region in the smooth Heaviside function is equal to 2α unit cells. An MMCS with n transient unit cells is denoted Tn MMCS.

To optimize the intermediate unit cells, bulk and shear moduli were chosen as the minimization objective, P_m, for HS and RH MMCSs, respectively. Fig. 6(a) illustrates the geometric configurations, and the variations in P_m and density of the unit cells in T13 HS and RH MMCSs mapped through a smooth Heaviside VCUTS. The (unmorphed) based and target unit cells are located on the left and right ends of each MMCS. Thus, these MMCSs show a clear change in morphology between the two unit cells. As shown in Fig. 6(a), smooth geometric transitions are obtained at the interfaces. In both HS and RH MMCSs, P_m monotonically increases following the same pattern as the VCUTS. Smooth density variations are observed for the HSG and RHG MMCSs, while the densities of the unit cells in the HSU and RHU MMCSs remain almost constant as expected.

The geometric configurations and variations in P_m and density of the unit cells in T13 HS and RH MMCSs mapped through a half-sine VCUTS are presented in Fig. 6(b). The (unmorphed) base unit cells are located on the left and right sides of the MMCSs. Smooth variations in P_m and density are observed. The pattern of the variations follows the VCUTS shape except in the case of the density of the HSU and RHU MMCSs, which remain constant as intended.

These numerical analyses demonstrate the ability of the proposed method to synthesize MMCSs that morph between two unit cell types with different shapes and topologies, simultaneously achieving smooth geometric transitions and stable variations of the unit cells' properties, the latter of which mostly follow the shape of the VCUTS applied.

3.2. Compressive mechanical property

Compression tests were conducted on cubical HSG and HSU MMCSs, composed of 6 × 6 unit cells. The side length of each MMCS was 42 mm. To interpret the MMCSs' mechanical behavior, FEA were performed on both HSG/HSU and RHU/RHG MMCSs with the same dimensions as the physical specimens, using ANSYS Mechanical APDL 2018. All MMCSs were synthesized with smooth Heaviside functions having different transition lengths (2α).

The HSG and HSU MMCS physical specimens were printed in plastic resin (EP400, Graphy, Seoul, Republic of Korea) using a digital light processing machine (SLASH PLUS, Uniz, San Diego, CA, USA). The remaining resin attached to the parts was washed for 15 min with isopropyl alcohol and cured for 1 h using an ultraviolet curing machine (CureM U201H, Graphy). All compression tests were conducted at room temperature (~20 °C using a universal testing machine (Allround-Line Z050, ZwickRoell, Ulm, Germany) set at a crosshead speed of 2 mm/min. To investigate the

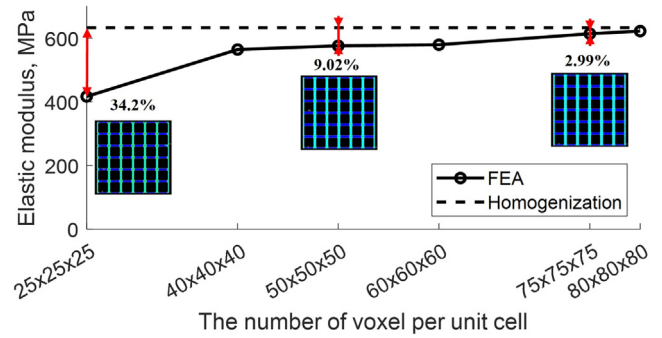**Fig. 8.** Results of the mesh sensitivity analysis on a cubical structure composed of 6 × 6 square unit cells.
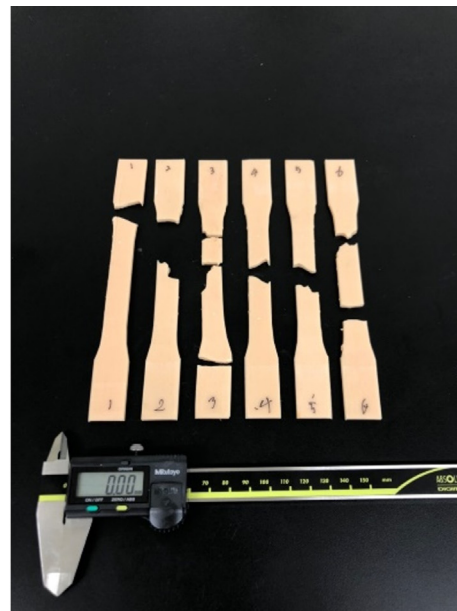

Fig. 7. EP400 specimens during (left) and after (right) standard tensile test.

effect of the manufacturing accuracy on the given conditions, the in-plane dimensions of each specimen were measured. These measurements were compared with the dimensions of the corresponding as-design models, finding a negligible difference of 0.041% on average.

To obtain the mechanical properties of the EP400 resin under the same manufacturing conditions, standard dog-bone coupons were subject to tensile tests according to the ASTM D638 Type 1 specifications, and additional compression tests were conducted at room temperature on 6 × 6 cubical honeycomb structures with a side length of 42 mm using a different universal testing machine (Allround-Line Z010, ZwickRoell) set a crosshead speed of 5 mm/min. Fig. 7 shows the EP400 dog-bone coupons during and after the tensile tests, which resulted in an elastic modulus of 2.66 GPa. Using this modulus and comparing the results from the compression tests with those from the corresponding FEA, the Poisson's ratio was estimated as 0.37. Details about the boundary conditions and material model are described in the following paragraph.

Each MMCS FEA model was tessellated using voxel-based finite elements of type SOLID 185 in ANSYS and assigned a linear isotro-

pic constitutive model [41]. As the accuracy of FEA depends on the resolution of the tessellation model, a mesh sensitivity analysis was conducted, whose results for the elastic modulus under uniform displacement along the vertical direction are shown in Fig. 8. The boundary conditions comprised a small uniform displacement applied to the top surface of the structure and frictionless contact between the bottom of the model and a rigid body. The total force applied to each element was obtained as the sum of the reaction forces [44,45]. The elastic modulus derived from the numerical homogenization [42] is also shown in Fig. 8 (dashed line). As the number of voxels per unit cell increases, the deviation between the two simulation values becomes smaller. The difference is less than 5% when the number of voxels per unit cell exceeds 75 × 75 × 75, corresponding to a mesh size of 0.093 mm. Consequently, all finite element models were tessellated with this mesh size.

3.2.1. HSG & HSU MMCSs

Fig. 9 illustrates the experimental and FEA results for the HSG, HSU, RHG and RHU MMCSs with different numbers of transient
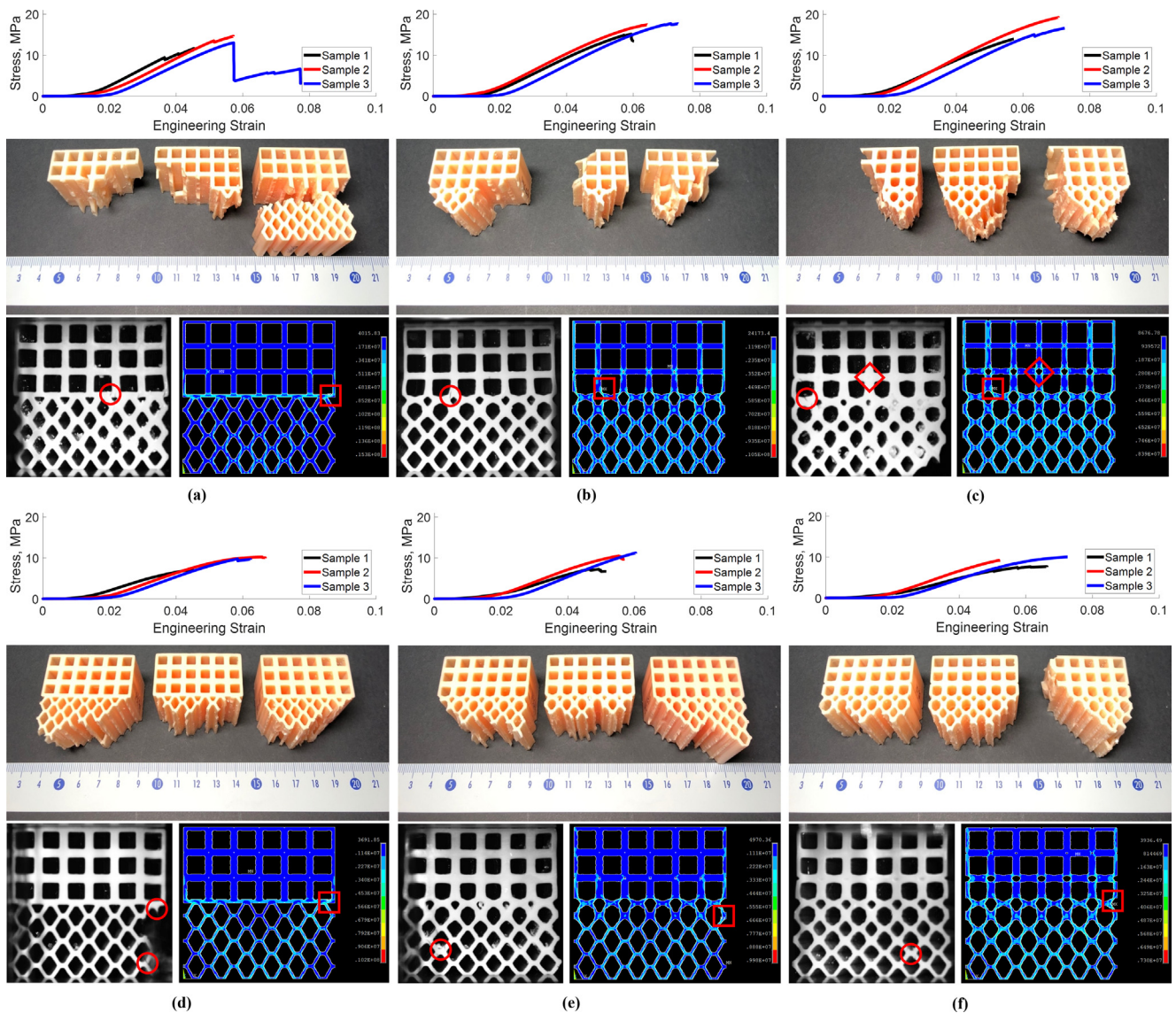

Fig. 9. Compression test results for HSU and HSG MMCS: (a) T0 HSU, (b) T3 HSU, (c) T6 HSU, (d) T0 HSG, (e) T3 HSG, and (f) T6 HSG. Each subfigure shows the stress–strain curve (top), the specimen after failure (middle), the deformation before fracture (bottom left), and the von Mises stress distribution at 0.1% strain (bottom right).

unit cells. Each of the six subfigures presented includes, from top to bottom, a stress–strain curve, the remnants of the specimen after the compression test, and images of deformed shape captured by a video extensometer (ZwickRoell) before the fracture (bottom left), and of the von Mises stress (Pa) distributions at 0.1% strain (bottom right). The number of transient unit cells n was set to 0, 3, and 6.

Red rectangular boxes show points where the maximum stress occurred. The stress was distributed near the interfaces and honeycomb region in T0 HSU and T0 HSG MMCSs, spreading over the structures as n became larger. Red circles present crack initiation points.

As summarized in Table 1, the maximum von Mises stress in the HSG and HSU MMCSs decreased by 28.4% and 45.1%, respectively, compared with that in the T0 MMCSs. The elastic modulus in the HSG MMCSs monotonically decreased by 303.0 MPa as n increased. However, in the HSU MMCSs, the moduli showed an enhancement and decrease as n increased. The major reason for this inconsistency is the geometric shrinkage in the transient regions, possibly

causing stress concentration. This can be prevented by increasing κ, which controls the minimum thickness of the microstructures.

Fig. 10 shows the average ultimate strengths of the HSU and HSG MMCSs, which were obtained from the experimental results omitting the worst cases. The average ultimate strengths of HSU and HSG MMCSs increased by 27.7% and 6.7%, respectively, compared to that of T0 HSU and T0 HSG MMCSs. Only T6 HSG MMCS presented a negligible decrease in the ultimate strength by 3.9%.
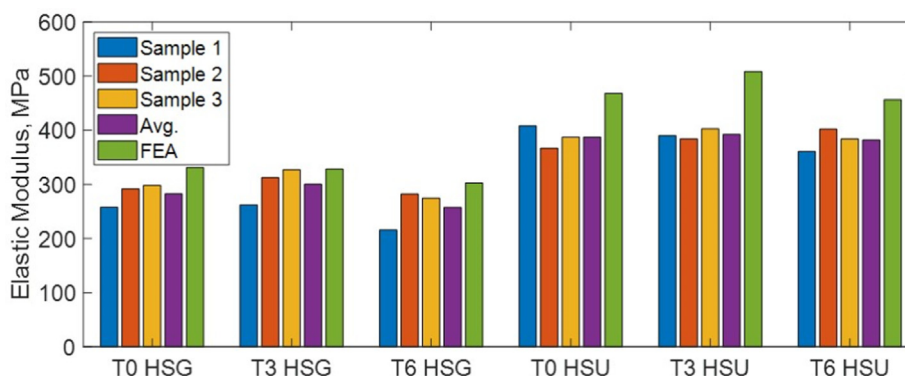
The elastic moduli obtained from the experiments and FEA are compared in Fig. 11. The average differences in the elastic modulus between experiments and FEA were 12.7% and 18.8% in HSG and HSU MMCSs, respectively. The major causes of these differences are assumed to be the 3D printing quality and inadequate structural geometry from the curing process. For example, a hole inside the diamond box shown in Fig. 9(c) was meant to be 1.96 × 1.96 mm. However, the feature was not correctly fabricated as designed. In addition, the extruded geometry was not suitable for the ultraviolet curing process due to occlusion to the interior caused by the external structure.

Table 1
Maximum von Mises stresses and elastic moduli of HS MMCSs obtained from FEA.

MMCS		Maximum von Mises stress		Elastic modulus	
		Stress (MPa)	Variation (%)	Modulus (MPa)	Variation (%)
HSG	T0	10.2	-	331.2	-
	T3	10.0	−2.0	328.5	−0.8
	T6	7.3	−28.4	303.0	−8.5
HSU	T0	15.3	–	468.4	–
	T3	10.5	−31.4	508.2	8.5
	T6	8.4	−45.1	456.6	−2.5
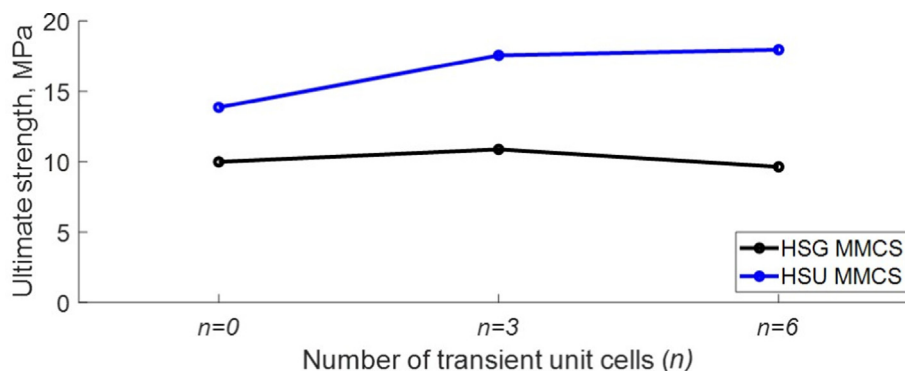
Fig. 10. Average ultimate strengths of HSG and HSU MMCSs with n = 0, 3, and 6.

Fig. 11. Elastic moduli of HSG and HSU MMCSs obtained from experiments and FEA.

3.2.2. RHG & RHU MMCSs

Unlike the HS MMCSs, the stress distribution of the RHG and RHU MMCSs showed different patterns in Fig. 12. The maximum von Mises stress, which occurred near the interfaces in the HS MMCSs, occurred in various locations in the re-entrant honeycomb region in the RHG MMCSs and honeycomb region in the RHU MMCSs. In addition, in Table 2, the corresponding stress values decreased by 3.8% and 35.5% in the RHG and RHU MMCSs, respectively, compared to the T0 RHG and RHU MMCS,

except in the T6 RHG MMCS, where the maximum stress increased by 10.1%. This can be explained by the density variations of the T6 RHG MMCS. As shown in Fig. 6, the densities of each unit cell change depending on the density gradient type and VCUTS shape. For the T6 RHG MMCS, the unit cells near the bottom have a relatively lower density than those in the middle. Thus, the structural thickness of these unit cells is thinner than in the other regions. This makes the stress in this region higher than in the others.
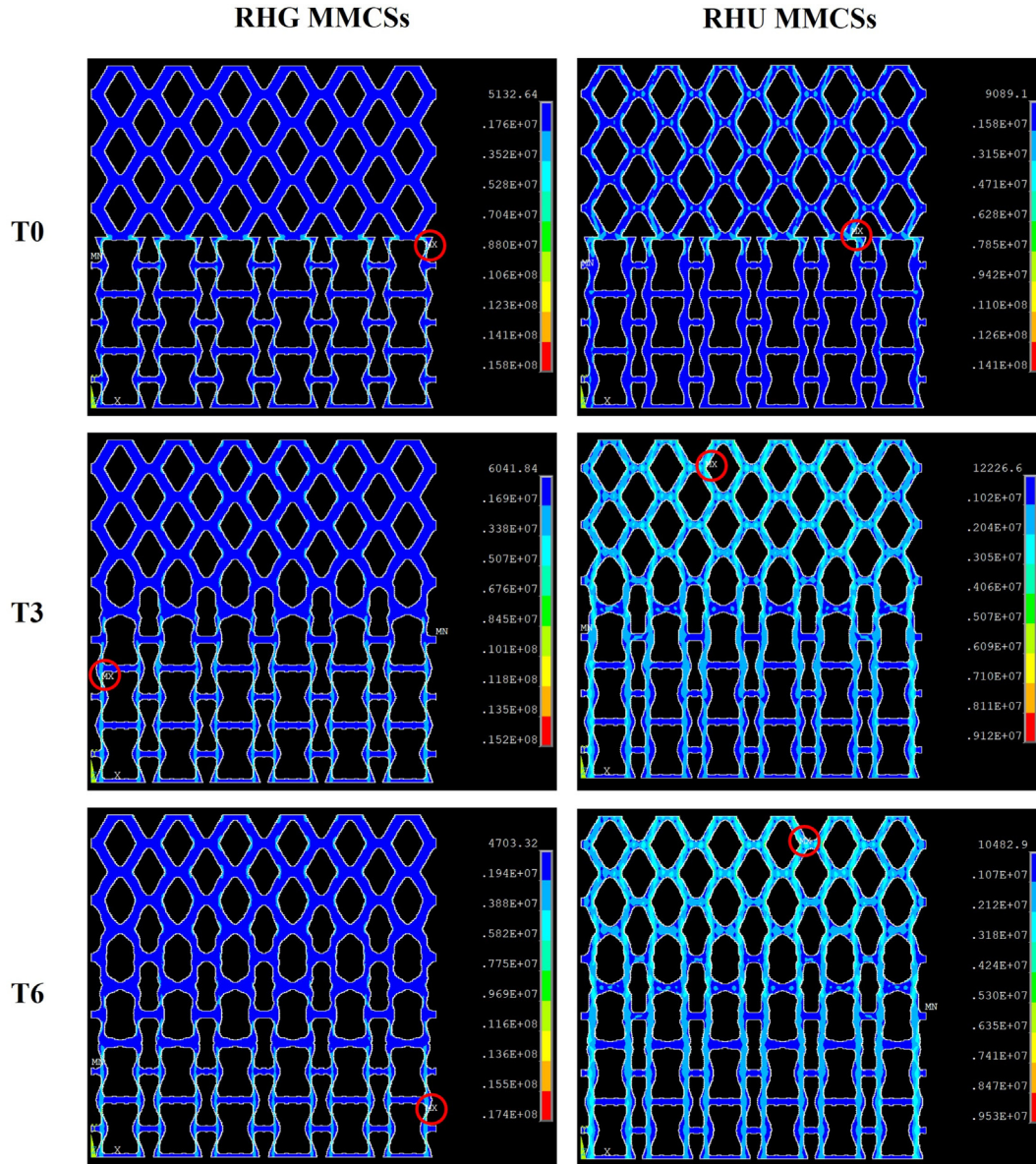

Fig. 12. Compression simulation results and stress distributions at 0.1% strain for RHG and RHU MMCSs with *n* = 0, 3, and 6.

Table 2
Maximum von Mises stresses and elastic moduli of RH MMCSs obtained from FEA.

MMCS		Maximum von Mises stress		Elastic modulus	
		Stress (MPa)	Variation (%)	Stress (MPa)	Variation (%)
RHG	T0	15.8	–	177.0	–
	T3	15.2	−3.8	269.5	52.3
	T6	17.4	10.1	316.3	78.7
RHU	T0	14.1	–	232.6	–
	T3	9.1	−35.5	322.0	38.4
	T6	9.5	−32.6	360.6	55.0

The elastic modulus in the RHG and RHU MMCSs increased by 78.7% and 55.0% compared with that of T0 RHG and RHU MMCS, respectively. This result indicates that one can make stiffer structures by applying the proposed method to the T0 RH MMCSs.

Overall, the compressive results show that the proposed design method can improve of the mechanical properties of the cellular structure depending on the type of base and target unit cells, density gradient, and the number of transient unit cells.

4. Conclusion

In this paper, an MMCS design method was proposed, which guarantees smooth connectivity and mechanical property variations between two unit cells. To synthesize MMCSs, the intermediate unit cells were optimized using a GA under geometric and mechanical constraints with the help of the parametric unit cell representation. Based on the intermediate unit cells, a level-set model was constructed by stacking the intermediate unit cells and interpolating their boundaries. The level-set model allows us to synthesize connectable MMCSs with a smooth VCUTS ensuring at least C^0 continuity at the interfaces and high degrees of freedom for MMCS internal shape [26]. Experiments and FEA were conducted to evaluate the mechanical behaviors and properties under the uniaxial compression conditions. In addition, the effect of the VCUTS shape on the geometric transitions and mechanical properties of MMCSs was investigated. The major findings of this study are summarized as follows:

- By adopting a VCUT level-set method with a customized level-set model for the MMCS design, smooth geometric transitions at the interfaces are verified between two unit cells with different density and topology. In addition, geometrically varying MMCSs can be synthesized by simply adjusting the VCUTS shape.
- Variations of the homogenized mechanical properties of unit cells in the MMCSs are consistent with the VCUTS shape, and density variations of unit cells are affected by densities of the base and target unit cells.
- By applying the proposed method, some structural performance enhancements are observed. The maximum stress of the MMCSs decreases by 45.1% compared with the MMCSs without a transient region, which are discontinuous at the interfaces. The elastic modulus and the ultimate strength increase by 78.7% and 27.7%, respectively.
- The structural performance is not proportional to the number of unit cells in the transient region, but varies depending on the types of unit cells, density gradients, VCUTS shape, and the number of unit cells in the transient region.
- In future, the proposed MMCS design method could be explored using multi-cellular structural optimization to simultaneously improve the performance and the robustness of structures.

The proposed method is applicable in 2D and 3D design spaces, but only 2D design examples were presented in this paper. To design an MMCS with 3D unit cells, careful adjustments are needed in the parametric unit cell representation process since the computational cost exponentially increases due to an increase in the number of reference points and geometric complexity for representing voids in 3D space.

CRediT authorship contribution statement

Youngdoo Kim: Conceptualization, Methodology, Software, Formal analysis, Investigation, Data curation, Writing – original draft, Visualization. **Phong C.H. Nguyen:** Software, Validation, Writing – review & editing. **Hoon Kim:** Validation, Investigation, Resources, Writing – review & editing. **Young Choi:** Supervision, Project administration, Writing – review & editing.

Declaration of Competing Interest

The authors declare that they have no known competing financial interests or personal relationships that could have appeared to influence the work reported in this paper.

Data Availability

The raw/processed data required to reproduce these findings cannot be shared at this time as the data also forms part of an ongoing study.

References

[1] J.C. Weaver, G.W. Milliron, A. Miserez, K. Evans-Lutterodt, S. Herrera, I. Gallana, W.J. Mershon, B. Swanson, P. Zavattieri, E. DiMasi, D. Kisailus, The stomatopod dactyl club: a formidable damage-tolerant biological hammer, Science 336 (6086) (2012) 1275–1280.

[2] U.G.K. Wegst, Bending efficiency through property gradients in bamboo, palm, and wood-based composites, J. Mech. Behav. Biomed. Mater. 4 (5) (2011) 744–755.

[3] Y. Zhang, W. Huang, C. Hayashi, J. Gatesy, J. McKittrick, Microstructure and mechanical properties of different keratinous horns, J. R. Soc. Interface 15 (143) (2018) 20180093, https://doi.org/10.1098/rsif.2018.0093.

[4] L.J. Gibson, Cellular solids, MRS Bull. 28 (4) (2003) 270–274.

[5] Q.T. Do, C.H.P. Nguyen, Y. Choi, Homogenization-based optimum design of additively manufactured Voronoi cellular structures, Addit. Manuf. 45 (2021). https://doi.org/10.1016/j.addma.2021.102057 102057.

[6] H.-Y. Lei, J.-R. Li, Z.-J. Xu, Q.-H. Wang, Parametric design of Voronoi-based lattice porous structures, Mater. Des. 191 (2020). https://doi.org/10.1016/j.matdes.2020.108607 108607.

[7] N. Ivarsson, M. Wallin, D.A. Tortorelli, Topology optimization for designing periodic microstructures based on finite strain viscoplasticity, Struct. Multidiscip. Optim. 61 (6) (2020) 2501–2521, https://doi.org/10.1007/s00158-020-02555-x.

[8] A. Clausen, F. Wang, J.S. Jensen, O. Sigmund, J.A. Lewis, Topology optimized architectures with programmable Poisson's ratio over large deformations, Adv. Mater 27 (37) (2015) 5523–5527.

[9] Y. Li, Z. Feng, L. Hao, L. Huang, C. Xin, Y. Wang, E. Bilotti, K. Essa, H. Zhang, Z. Li, A review on functionally graded materials and structures via additive manufacturing: from multi-scale design to versatile functional properties, Advanced Materials Technologies 5 (6) (2020) 1900981.

[10] Z. Liu, M.A. Meyers, Z. Zhang, R.O. Ritchie, Functional gradients and heterogeneities in biological materials: Design principles, functions, and bioinspired applications, Prog. Mater Sci. 88 (2017) 467–498.

[11] O. Sigmund, Materials with prescribed constitutive parameters: an inverse homogenization problem, Int. J. Solids Struct. 31 (17) (1994) 2313–2329, https://doi.org/10.1016/0020-7683(94)90154-6.

[12] J.K. Guest, J.H. Prévost, Design of maximum permeability material structures, Comput. Methods Appl. Mech. Eng. 196 (4–6) (2007) 1006–1017, https://doi.org/10.1016/j.cma.2006.08.006.

[13] J.K. Guest, J.H. Prévost, Optimizing multifunctional materials: design of microstructures for maximized stiffness and fluid permeability, Int. J. Solids Struct. 43 (22–23) (2006) 7028–7047, https://doi.org/10.1016/j.ijsolstr.2006.03.001.

[14] O. Sigmund, S. Torquato, I.A. Aksay, On the design of 1–3 piezocomposites using topology optimization, J. Mater. Res. 13 (4) (1998) 1038–1048, https://doi.org/10.1557/JMR.1998.0145.

[15] P. Wei, Z. Li, X. Li, M.Y. Wang, An 88-line MATLAB code for the parameterized level set method based topology optimization using radial basis functions, Struct. Multidiscip. Optim. 58 (2) (2018) 831–849, https://doi.org/10.1007/s00158-018-1904-8.

[16] J.S. Choi, T. Yamada, K. Izui, S. Nishiwaki, J. Yoo, Topology optimization using a reaction–diffusion equation, Comput. Methods Appl. Mech. Eng. 200 (29–32) (2011) 2407–2420, https://doi.org/10.1016/j.jmbbm.2011.02.013.

[17] X. Wang, Y. Mei, M.Y. Wang, Level-set method for design of multi-phase elastic and thermoelastic materials, Int. J. Mech. Mater. Des. 1 (3) (2004) 213–239, https://doi.org/10.1007/s10999-005-0221-8.

[18] C. Zhuang, Z. Xiong, H. Ding, Bézier extraction based isogeometric approach to multi-objective topology optimization of periodic microstructures, Int. J. Numer. Meth. Eng. 122 (23) (2021) 6827–6866, https://doi.org/10.1002/nme.6813.

[19] H. Deng, S. Hinnebusch, A.C. To, Topology optimization design of stretchable metamaterials with Bézier skeleton explicit density (BSED) representation algorithm, Comput. Methods Appl. Mech. Eng. 366 (2020) 113093, https://doi.org/10.1016/j.cma.2020.113093.

[20] M. Yang, A. Nagarajan, B. Liang, S. Soghrati, New algorithms for virtual reconstruction of heterogeneous microstructures, Comput. Methods Appl. Mech. Eng. 338 (2018) 275–298, https://doi.org/10.1016/j.cma.2018.04.030.

[21] X. Kou, S. Tan, Microstructural modelling of functionally graded materials using stochastic Voronoi diagram and B-Spline representations, Int. J. Comput. Integr. Manuf. 25 (2) (2012) 177–188, https://doi.org/10.1080/0951192X.2011.627948.

[22] C.H.P. Nguyen, Y. Kim, Y. Choi, Design for Additive Manufacturing of Functionally Graded Lattice Structures: A Design Method with Process Induced Anisotropy Consideration, International Journal of Precision Engineering and Manufacturing-Green Technology 8 (1) (2021) 29–45, https://doi.org/10.1007/s40684-019-00173-7.

[23] C.H.P. Nguyen, Y. Choi, Multiscale design of functionally graded cellular structures for additive manufacturing using level-set descriptions, Struct. Multidiscip. Optim. 64 (4) (2021) 1983–1995, https://doi.org/10.1007/s00158-021-02959-3.

[24] H. Li, Z. Luo, N. Zhang, L. Gao, T. Brown, Integrated design of cellular composites using a level-set topology optimization method, Comput. Methods Appl. Mech. Eng. 309 (2016) 453–475, https://doi.org/10.1016/j.cma.2016.06.012.

[25] J. Alexandersen, B.S. Lazarov, Topology optimisation of manufacturable microstructural details without length scale separation using a spectral coarse basis preconditioner, Comput. Methods Appl. Mech. Eng. 290 (2015) 156–182, https://doi.org/10.1016/j.cma.2015.02.028.

[26] H. Liu, H. Zong, T. Shi, Q. Xia, M-VCUT level set method for optimizing cellular structures, Comput. Methods Appl. Mech. Eng. 367 (2020). https://doi.org/10.1016/j.cma.2020.113154 113154.

[27] H. Zong, H. Liu, Q. Ma, Y.e. Tian, M. Zhou, M.Y. Wang, VCUT level set method for topology optimization of functionally graded cellular structures, Comput. Methods Appl. Mech. Eng. 354 (2019) 487–505.

[28] X. Liu, L. Gao, M. Xiao, Y. Zhang, Kriging-assisted design of functionally graded cellular structures with smoothly-varying lattice unit cells, Comput. Methods Appl. Mech. Eng. 390 (2022). https://doi.org/10.1016/j.cma.2021.114466 114466.

[29] Y. Wang, F. Chen, M.Y. Wang, Concurrent design with connectable graded microstructures, Comput. Methods Appl. Mech. Eng. 317 (2017) 84–101, https://doi.org/10.1016/j.cma.2016.12.007.

[30] O. Al-Ketan, R.K. Abu Al-Rub, MSLattice: A free software for generating uniform and graded lattices based on triply periodic minimal surfaces,

[31] O. Al-Ketan, D.-W. Lee, R. Rowshan, R.K. Abu Al-Rub, Abu Al-Rub, Functionally graded and multi-morphology sheet TPMS lattices: Design, manufacturing, and mechanical properties, J Mech Behav Biomed Mater 102 102 (2020) 103520, https://doi.org/10.1016/j.jmbbm.2019.103520.

[32] I. Maskery, A.O. Aremu, L. Parry, R.D. Wildman, C.J. Tuck, I.A. Ashcroft, Effective design and simulation of surface-based lattice structures featuring volume fraction and cell type grading, Mater. Des. 155 (2018) 220–232, https://doi.org/10.1016/j.matdes.2018.05.058.

[33] F. Liu, Z. Mao, P. Zhang, D.Z. Zhang, J. Jiang, Z. Ma, Functionally graded porous scaffolds in multiple patterns: New design method, physical and mechanical properties, Mater. Des. 160 (2018) 849–860, https://doi.org/10.1016/j.matdes.2018.09.053.

[34] S. Zhou, Q. Li, Design of graded two-phase microstructures for tailored elasticity gradients, J. Mater. Sci. 43 (15) (2008) 5157–5167, https://doi.org/10.1007/s10853-008-2722-y.

[35] P. Liu, Z. Kang, Y. Luo, Two-scale concurrent topology optimization of lattice structures with connectable microstructures, Addit. Manuf. 36 (2020) 101427, https://doi.org/10.1016/j.addma.2020.101427.

[36] H. Li, Z. Luo, L. Gao, P. Walker, Topology optimization for functionally graded cellular composites with metamaterials by level sets, Comput. Methods Appl. Mech. Eng. 328 (2018) 340–364, https://doi.org/10.1016/j.cma.2017.09.008.

[37] Z. Du, X.-Y. Zhou, R. Picelli, H.A. Kim, Connecting Microstructures for Multiscale Topology Optimization With Connectivity Index Constraints, J. Mech. Des. 140 (11) (2018), https://doi.org/10.1115/1.4041176.

[38] A. Radman, X. Huang, Y. Xie, Topology optimization of functionally graded cellular materials, J. Mater. Sci. 48 (4) (2013) 1503–1510, https://doi.org/10.1007/s10853-012-6905-1.

[39] E. Garner, H.M.A. Kolken, C.C.L. Wang, A.A. Zadpoor, J. Wu, Compatibility in microstructural optimization for additive manufacturing, Addit. Manuf. 26 (2019) 65–75, https://doi.org/10.1016/j.addma.2018.12.007.

[40] S.M.T. Zobaer, A. Sutradhar, An energy-based method for interface connectivity of incompatible microstructures through parametric modeling, Comput. Methods Appl. Mech. Eng. 370 (2020) 113278, https://doi.org/10.1016/j.cma.2020.113278.

[41] C.H.P. Nguyen, Y. Kim, Q.T. Do, Y. Choi, Implicit-based computer-aided design for additively manufactured functionally graded cellular structures, J. Comput. Des. Eng. 8 (3) (2021) 813–823, https://doi.org/10.1093/jcde/qwab016.

[42] G. Dong, Y. Tang, Y.F. Zhao, A 149 line homogenization code for three-dimensional cellular materials written in matlab, J. Eng. Mater. Technol. 141 (1) (2019).

[43] S. Liu, Q. Li, J. Liu, W. Chen, Y. Zhang, A Realization Method for Transforming a Topology Optimization Design into Additive Manufacturing Structures, Engineering 4 (2) (2018) 277–285, https://doi.org/10.1016/j.eng.2017.09.002.

[44] X. Li, M. Ghasri-Khouzani, A.-A. Bogno, J. Liu, H. Henein, Z. Chen, A.J. Qureshi, Investigation of compressive and tensile behavior of stainless steel/dissolvable aluminum bimetallic composites by finite element modeling and digital image correlation, Materials 14 (13) (2021) 3654.

[45] M. Helou, S. Vongbunyong, S. Kara, Finite element analysis and validation of cellular structures, Procedia CIRP 50 (2016) 94–99.

Material Design & Processing, Communications (2020), https://doi.org/10.1002/mdp2.205.